ACS APPLIED MATERIALS & INTERFACES

Article

Isolating the photovoltaic junction: atomic layer deposited TiO-RuO alloy Schottky contacts for silicon photoanodes

Olivia L. Hendricks, Andrew G. Scheuermann, Michael Schmidt, Paul K. Hurley, Paul C McIntyre, and Christopher E. D. Chidsey

ACS Appl. Mater. Interfaces, **Just Accepted Manuscript** • DOI: 10.1021/acsami.6b08558 • Publication Date (Web): 22 Aug 2016

Just Accepted

ACS Publications

ACS Applied Materials & Interfaces is published by the American Chemical Society.
1155 Sixteenth Street N.W., Washington, DC 20036

Isolating the photovoltaic junction: atomic layer deposited TiO_2-RuO_2 alloy Schottky contacts for silicon photoanodes

Olivia L. Hendricks,[†] Andrew G. Scheuermann,[‡] Michael Schmidt,[§] Paul K. Hurley,[§] Paul C. McIntyre,[‡] Christopher E. D. Chidsey[*†]*

† Department of Chemistry, Stanford University, Stanford, California 94305, United States

‡Department of Materials Science and Engineering, Stanford University, Stanford, California, 94305, United States

§Tyndall National Institute, University College Cork, Cork, Ireland

KEYWORDS: atomic layer deposition, Schottky junctions, MIS junctions, photoanodes, photovoltage, TiO_2 alloys

ABSTRACT: We have synthesized nanoscale TiO_2-RuO_2 alloys by atomic layer deposition (ALD) that possess a high work function and are highly conductive. As such, they function as good Schottky contacts to extract photogenerated holes from n-type silicon while simultaneously interfacing with water oxidation catalysts. The ratio of TiO_2 to RuO_2 can be precisely controlled by the number of ALD cycles for each precursor. Increasing the composition above 16% Ru sets the electronic conductivity and the metal work function. No significant Ohmic loss for hole

transport is measured as film thickness increases from 3 to 45 nm for alloy compositions ≥ 16% Ru. Silicon photoanodes with a 2 nm surface SiO_2 layer that are coated by these alloy Schottky contacts having compositions in the range of 13-46% RuO_2 exhibit average photovoltages of 525 mV, with a maximum photovoltage of 570 mV achieved. Depositing TiO_2-RuO_2 alloys on nSi sets a high effective work function for the Schottky junction with the semiconductor substrate, thus generating a large photovoltage that is isolated from the properties of an overlying oxygen evolution catalyst or protection layer.

1. INTRODUCTION: Metal-insulator-semiconductor (MIS) structures are promising candidates for integrated solar driven water splitting devices.[1,2] The photovoltage produced by an MIS junction depends on the strength of the built-in field, or Schottky barrier height. This built-in field, in turn, depends on the difference in work function between the semiconductor and the metal, taking charges and interface fields into account.[3] In the 1970s, Green and co-workers found that a conductor with a sufficiently high work function produced a surface inversion layer at the semiconductor/insulator interface that helped screen interface traps and promote minority carrier transport across the insulator. As long as the insulator was kept sufficiently thin (1-3 nm), it could simultaneously enable interface defect passivation and facile charge transport by tunneling.[3–6] In recent examples of this approach for water oxidation, the metal layer has both set the built-in field to extract photogenerated carriers from the semiconductor and also functioned as the catalyst for water oxidation.

Recent advances in atomic layer deposition (ALD) of metal oxide protection layers have made it possible to suppress oxidative corrosion of semiconductor materials, such as silicon, that would

otherwise be unstable under the conditions required for water oxidation.[1,2,7–13] Incorporation of such protection layers into the MIS junction, however, has compromised the photovoltages commonly reported for these devices. An ideal MIS junction using silicon has a theoretical maximum open circuit voltage of 700-800 mV.[14] Previous reports of silicon MIS photoanodes, however, have fallen well below this benchmark. For example, nSi photoanodes protected by highly conductive TiO_2 have reported photovoltages of ~400 mV,[2] with some devices only achieving 200-250 mV.[13]

Although TiO_2 is highly stable under the conditions required for water oxidation,[15] its electrical properties are difficult to control and are not ideal for simultaneously generating the maximum photovoltage at high photocurrent.[12] The conductivity of TiO_2 films reported by different research groups has been inconsistent, even in cases where the same precursor species and similar temperatures and pressures are used in ALD film deposition.[2,11] Evidently, the factors controlling TiO_2 conductivity in ultrathin and amorphous or weakly-crystalline ALD-grown films are not easily controlled. Moreover, the TiO_2 causes photovoltage losses regardless of its hole-conducting capabilities.[12] If the TiO_2 is highly conductive, it should set the built-in field in the semiconductor. Highly-conductive n-type TiO_2 is expected to have a work function near its conduction band edge, leading to a small built-in field with nSi. Conversely, if the TiO_2 behaves as an insulator, increasing its thickness leads to photovoltage losses from a charge extraction barrier at the semiconductor/insulator interface.[12]

We have optimized the electrical properties of TiO_2 by alloying it with RuO_2 in an all-ALD process to make a highly conductive, high work function Schottky contact to n-type silicon. Our

work was motivated by the success of the dimensionally stable anode (DSA) for industrial chlorine evolution, which occurs at similarly positive potentials to water oxidation.[16–18] Today's DSAs consist of a thick (a few microns), mixed TiO_2/RuO_x coating prepared by thermal decomposition of appropriate precursors at high temperature. The resulting electrode is known for its high conductivity and durability.[16–18] We sought to create an ultra-thin analogue to the DSA and to understand the chemical and electrical properties of similar TiO_2-RuO_2 alloys prepared by ALD.

As illustrated in Figure 1, the TiO_2-RuO_2 alloy/SiO_2/n-type silicon junction functions as an isolated MIS photoanode. Isolating the photovoltaic junction from the electronic characteristics of the catalyst or from overlying protection layers allows for optimization of the latter components for catalytic efficiency and stability without compromising the photovoltage or photocurrent of the MIS junction. Alloyed TiO_2-RuO_2 films are efficient hole conducting contacts to silicon and possess a high work function of 5-5.2 eV. Alloys ranging from 13-46% Ru showed an average photovoltage of 525 mV, with a maximum observed photovoltage of 570 mV. This is a significant improvement over previously reported electrodes with similarly conductive but non-alloyed TiO_2. Hole conduction through the films shows no significant Ohmic loss as film thickness is increased from 3 to 45 nm. Thus, nanoscale RuO_2-TiO_2 alloys provide Schottky junction photoanodes with both high conductance and high photovoltage, independent of film thickness. Most importantly, the built-in-field is set by the TiO_2-RuO_2 alloy, not by the overlying catalyst.

This work illustrates the significant opportunity presented by alloyed and structured ALD metal oxide films to control and isolate the properties of Schottky contacts to semiconductors. Alloying by ALD enables the flexibility to incorporate a wide variety of materials that could, in principle, be optimized for any semiconductor absorber. This is particularly significant for semiconductors that cannot be doped to form high-quality homojunctions. Previous work has demonstrated that ALD CoO_x can be used to make a good Schottky contact to n-type silicon, and photovoltages greater than 500 mV were observed.[10] Similarly high photovoltages, however, were not observed when ALD NiO_x and FeO_x were used instead, despite similar reported work functions among these materials.[19,20] These inconsistencies suggest that further study is needed to understand the requirements for these types of Schottky contacts. Here, we present a rigorous characterization of TiO_2-RuO_2 alloys as model Schottky contacts to n-type silicon.

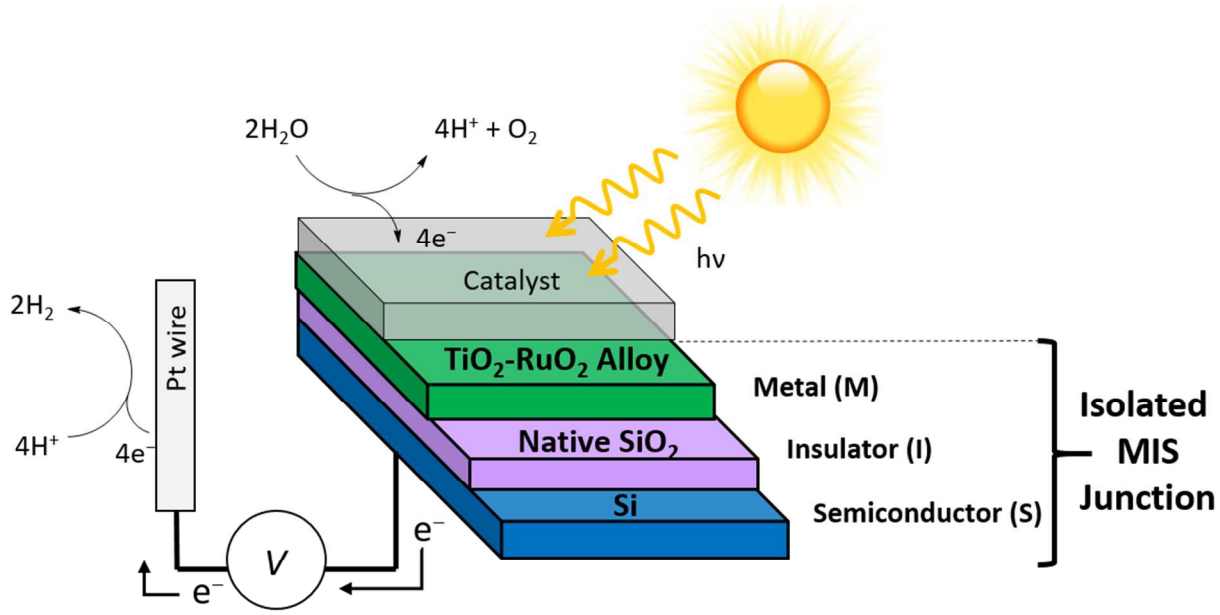

Figure 1. Schematic of the silicon photoanodes fabricated in this study using an isolated MIS junction. The TiO_2-RuO_2 alloy is sufficiently conductive to function as the metal. The native SiO_2, which is approximately 1.5-2 nm in thickness, is the insulator.

2. RESULTS AND DISCUSSION:

2.1 CHARACTERIZATION OF TiO_2-RuO_2 ALLOY FILMS

TiO_2 films were grown using half-cycle dosing of tetrakis-(dimethylamido)titanium (TDMAT) and water vapor.[21] RuO_x films were grown using bis(2,4-dimethylpentadienyl) ruthenium ($Ru(DMPD)_2$) and oxygen.[22,23] ALD of ruthenium is known to produce a range of oxidation states.[22–28] For now, we will refer to the oxidation state of ruthenium in our ALD films as RuO_x to preserve generality. TiO_2-RuO_x alloyed films were grown by an ALD alloying process in which individual cycles of TiO_2 and Ru were alternated. The ratio of TiO_2 to RuO_x cycles was chosen to control the Ru content in the film, and this cycle ratio was repeated for a designated number of ALD super-cycles. For example, one super-cycle of a 1:4 alloy would include one ALD cycle of TiO_2 followed by four ALD cycles of RuO_x. This process was repeated for multiple super-cycles to vary the film thickness.

Figure 2 shows atomic layer deposition data for **(A)** TiO_2, **(B)** RuO_x, and **(C)** TiO_2-RuO_x alloyed films. The TiO_2 film thickness was measured by ellipsometry. As seen in **Figure 2A,** TiO_2 film thickness increases linearly with the number of ALD cycles, and the growth per cycle is calculated to be ~0.5 Å/cycle. Ru film thickness was calculated using X-ray photoelectron spectroscopy (XPS) based on the silicon peak attenuation by the ruthenium overlayer. The details of these calculations are described in the Supporting Information. As seen in **Figure 2B,** Ru film thickness increases linearly with the number of ALD cycles. The growth per cycle is 0.5 Å/cycle, which is higher than previously reported for ruthenium ALD.[22–28] There is an initiation delay of approximately 10 cycles before steady-state ALD of Ru is achieved. This delay is quite low compared to typical noble metal ALD, which often exhibits > 50-100 cycles of initiation delay.

TiO_2-RuO_x alloyed film thicknesses were calculated using X-ray reflectivity (XRR), and the thickness of select samples was confirmed by transmission electron microscopy (TEM) (**Figure S5**). **Figure 2C** shows the % Ru incorporation relative to Ti calculated from XPS for alloyed films fabricated for several different TiO_2-RuO_x ALD cycle ratios. As expected, the % Ru content increases as the relative number of Ru cycles increases. An 8:1 TiO_2 to RuO_x cycle ratio results in 13% Ru, while a 1:4 TiO_2 to Ru cycle ratio yields 46% Ru. The % Ru content is highly reproducible, as well. Thus, the ALD alloying process can produce films over a wide composition range with very precise control over the Ru composition.

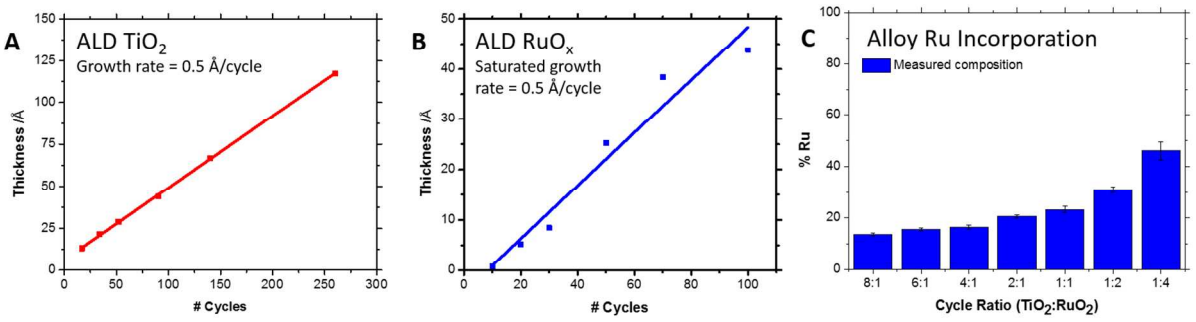

Figure 2. **(A)** Film thickness as a function of the number of ALD cycles for the TiO_2 ALD process **(B)** Film thickness as a function of the number of ALD cycles for the RuO_x ALD process. **(C)** The fraction of Ru incorporation into the TiO_2-RuO_x alloyed films as a function of ALD cycle ratio. The % Ru was calculated taking only Ru and Ti into consideration, ie % Ru = Ru / (Ru + Ti). Error bars reflect the standard deviation in % Ru. Film thickness for pure TiO_2 films was measured using ellipsometry. Film thickness for RuO_x films was determined by XPS.

Figure 3 shows high resolution XPS spectra for **(A)** a 5 nm TiO_2 film and (**B**) and a 4 nm Ru film. Details of the peak assignments and peak fitting procedures are described in the Supporting Information. Thin ALD films were chosen for analysis so that the substrate Si peaks were

detectable. All peak positions are referenced to the Si 2p peak at 99 eV. **Table 1** summarizes the calculated atomic compositions.

The Ti 2p spectrum in **Figure 3A** shows two peaks at 458.9 eV and 464.7 eV corresponding to the Ti $2p_{3/2}$ and Ti $2p_{1/2}$ peaks, respectively. The O1s peak shows three major components. The lowest binding energy component at 530.3 eV corresponds to oxygen in TiO_2,[29] while the highest binding energy component at 532.0 eV corresponds to oxygen in SiO_2.[30] The component at 531.2 eV is associated with carbon-bound oxygen. Based on the integrated areas under the Ti 2p peak and the O 1s component at 530.3 eV, the ratio of Ti to O was calculated to be 1:2, or fully oxidized TiO_2. No evidence of other Ti oxidation states were observed, particularly $Ti,^{3+}$ which would appear as a shoulder at lower binding energy in the Ti 2p spectrum.

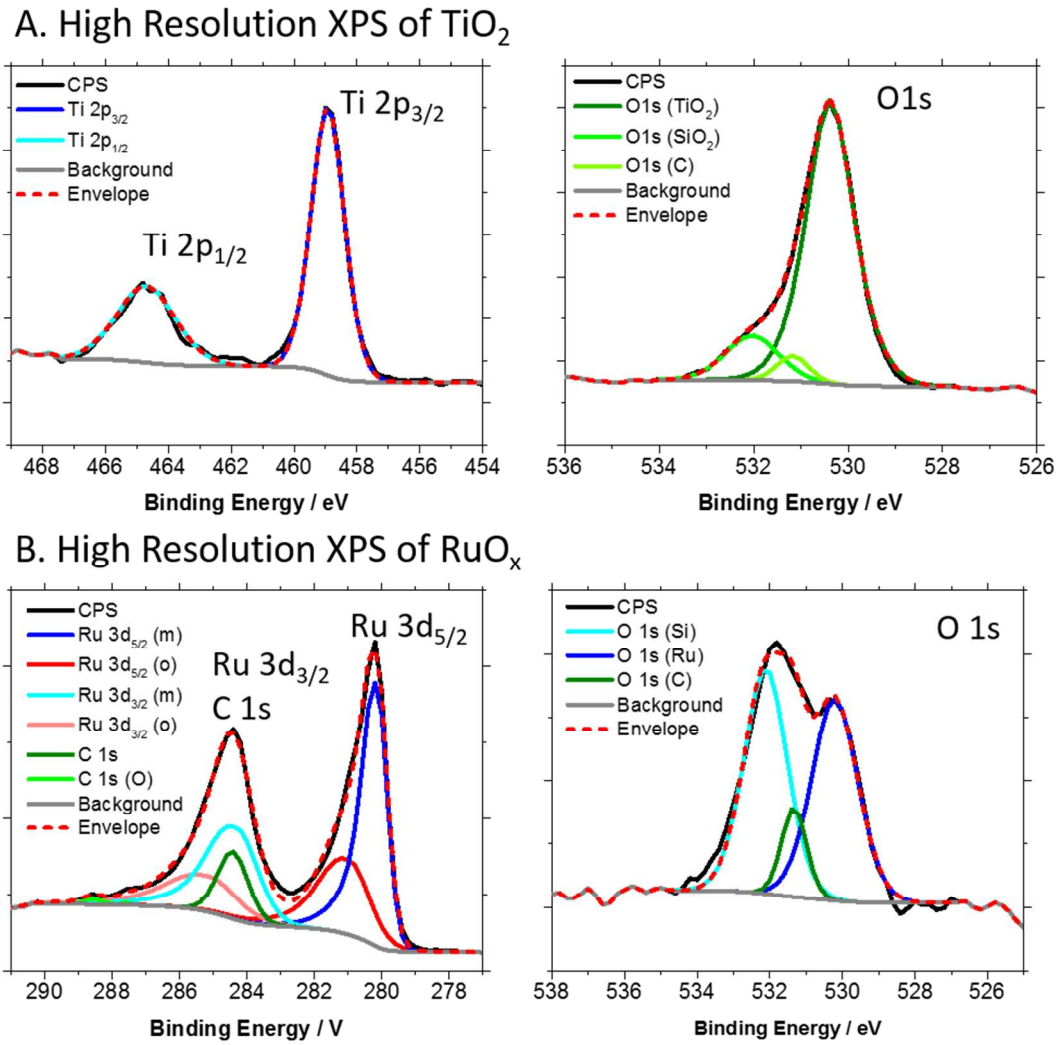

Figure 3. High resolution XPS spectra for **(A)** a 5 nm TiO_2 film on Si and **(B)** a 4 nm RuO_x film on Si. Lower binding energy peaks associated with metallic Ru are denoted (m) and typically have a smaller full width at half max. Higher binding energy peaks associated with oxidized Ru are denoted (o) and typically have a larger full width at half max. The specific binding energy of the oxide peaks suggests hydrated RuO_2.

The RuO_x 3d spectrum in **Figure 3B** was fit with six components: two Ru $3d_{5/2}$ peaks and their associated $3d_{3/2}$ peaks, adventitious C 1s at 284.4 eV, and higher binding energy C 1s peaks for

carbon-oxygen species. The lower binding energy Ru $3d_{5/2}$ peak at 280.1 eV corresponds to metallic Ru, while the higher binding energy Ru $3d_{5/2}$ peak at 281.0 eV corresponds to RuO_2.[31,32] The binding energy of the RuO_2 peak suggests that the oxide is hydrated. Hydrated RuO_2 typically appears at higher binding energy, ≥ 280.8 eV, whereas anhydrous RuO_2 appears closer to 280.6 eV.[31] RuO_2 is known to have a high affinity for water, even under ultra-high vacuum conditions.[33,34]

The O1s spectrum was fit with three components. Peaks at 532.0 eV and 531.1 eV are associated with SiO_2 and carbon-bound oxygen, respectively. These peaks appear at the same binding energy as in the O 1s spectrum for TiO_2. The lowest binding energy peak at 530.2 eV corresponds to oxygen in RuO_2. Its binding energy also suggests hydrated RuO_2, as the O1s peak for anhydrous RuO_2 typically appears at 529.4 eV.[31,32]

Table 1. Atomic % calculated from integrated areas of high resolution XPS spectra, scaled according to the appropriate relative sensitivity factors (RSF).

Atom	Atom % in ALD TiO_2	Atom % in ALD RuO_x	Atomic % in 33% Ru ALD alloy
Ru (metallic)	-	13.4	-
Ru (oxide)	-	7.3	5.8
Ti	22.1	-	11.4
C	19.6	32.0	29.2
O (Si)	7.4	14.0	9.2
O (Ru)	-	13.4	12.5

O (C)	1.2	3.2	1.6
O (Ti)	44.3	-	22.5
Si (metal)	1.7	8.9	3.2
Si (SiO_2)	3.7	6.9	4.6

Depth profiling analysis indicates that RuO_2 is only present at the surface of the ALD-Ru film (**Figure S8**). It is worth noting that ALD of Ru commonly results in a metallic film, with highly oxidizing conditions (high P_{O2}, long O_2 exposure time, O_2 plasma, ozone, etc.) required to deposit RuO_2.[22–28] This is typically attributed to the slow kinetics of oxygen diffusion through Ru films, and the requirement that a subsurface oxygen layer form during the ALD process to generate RuO_2.[22,35,36] Attempts to deposit RuO_2 directly in our ALD reactor using higher partial pressures of O_2 have so far been unsuccessful.

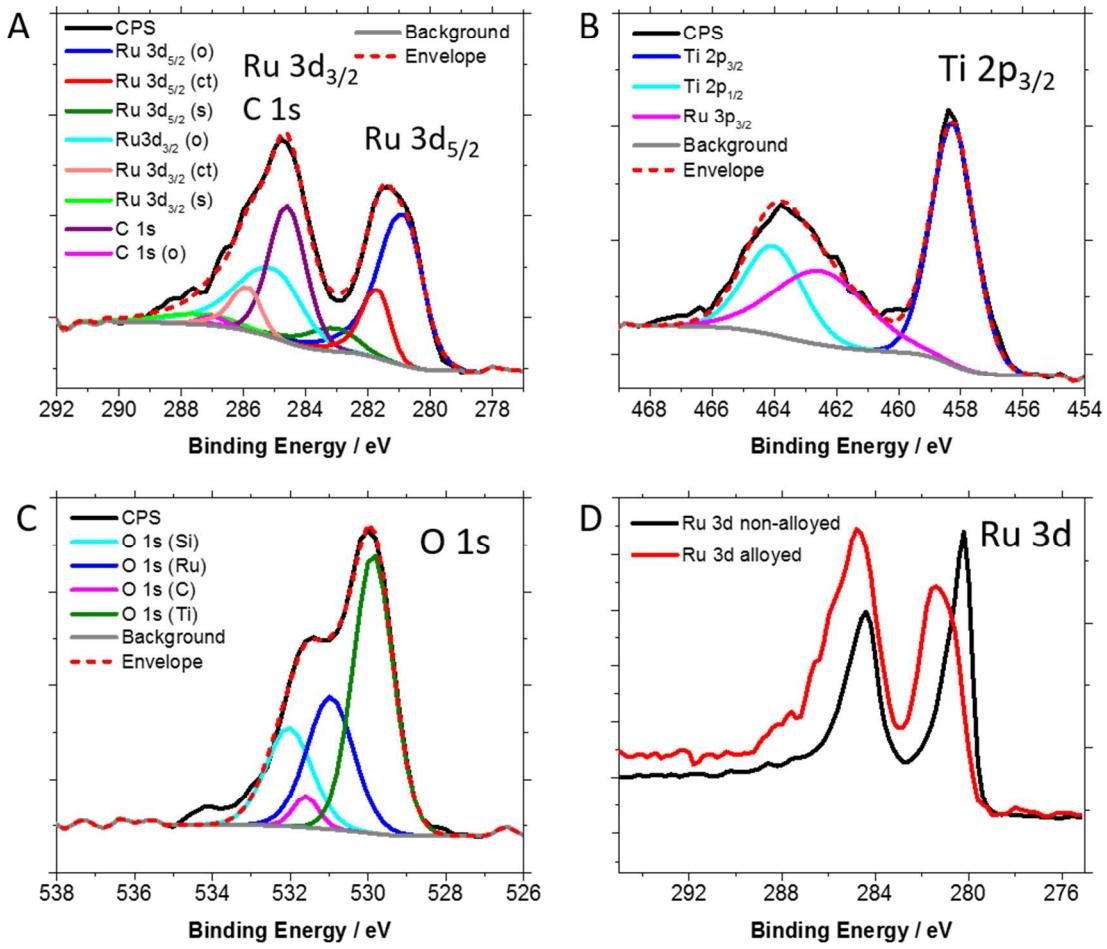

Figure 4. Representative high resolution XPS spectra for 6 nm 33% RuO_x alloy. **(A)** Ru 3d peak and its various components. Peaks associated with oxidized Ru are denoted (o), peaks associated with a potential charge transfer between Ru and Ti are denoted (ct), and satellite peaks are denoted (s). **(B)** Ti 2p peak and its various components, including the overlapping Ru $3p_{3/2}$ peak **(C)** O 1s peak and its various components **(D)** Comparison of the Ru 3d spectra in a 6 nm 33% RuO_x alloy film vs a 4 nm RuO_x film.

Figure 4 shows representative XPS spectra for a 6 nm 33% Ru alloy film. As shown in **Figure 4A**, the Ru 3d spectrum was fit with three Ru $3d_{5/2}$ peaks, their associated Ru $3d_{3/2}$ peaks, and the

same series of C 1s peaks. In this case, however, the lowest energy Ru $3d_{5/2}$ peak at 280.8 eV corresponds to oxidized RuO_2 instead of metallic Ru.[31,32] The highest binding energy Ru $3d_{5/2}$ peak at 283 eV and its corresponding Ru $3d_{3/2}$ peak are most likely satellite peaks, commonly observed in RuO_2 spectra due to core-hole screening.[33] There are two possible justifications for the middle Ru $3d_{5/2}$ component at 281.6 eV. One possibility is that this component represents hydrated RuO_2. Alternatively, this component could indicate a partial shift of the Ru $3d_{5/2}$ peak to higher binding energy. Previous literature reports have suggested that such a shift reflects charge transfer from Ru to Ti.[37] In this case, the Ru 3d shift to higher binding energy would be accompanied by a shift to lower binding energy in the Ti 2p spectrum. In fact, the Ti $2p_{3/2}$ peak in the 33% Ru alloy indeed shifts to lower binding energy, appearing at 458.3 eV instead of the 458.9 eV measured for non-alloyed TiO_2. Thus, it seems likely that charge transfer between Ru and Ti is occurring, supporting a solid solution model for TiO_2-RuO_2 alloys.

Table 1 lists the calculated atomic % for the components of the 33% Ru alloy film. The oxide stoichiometries are calculated to be $RuO_{2.1}$ and $TiO_{1.9}$. Thus, both Ti and Ru appear to be fully oxidized. Comparing the Ru 3d spectrum in the alloyed samples to the non-alloyed ruthenium samples also suggests a different oxidation state of ruthenium in the alloyed samples, as shown in **Figure 4D**. The Ru 3d peaks are broader and have shifted to higher binding energy by 1 eV compared to the ALD-Ru film, signifying a more oxidized chemical state.[22,31,32,37] Under ALD conditions, the presence of TiO_2 appears to favor the deposition of RuO_2 over metallic Ru.

To further investigate the distribution of Ru ions in the TiO_2 matrix, scanning Auger electron spectroscopy (AES) was performed to generate 2D elemental maps for a 15 nm 16% Ru alloy

and a 60 nm 46% Ru alloy (**Figure S9**). There appears to be no long-range phase separation between the TiO_2 and RuO_2 in these films. At the beam resolution limit of approximately 25 nm, no discrete areas of TiO_2 or RuO_2 are observed.

The structure of these films was also characterized by grazing incidence X-ray diffraction (GIXRD). GIXRD patterns from a series of films ranging in composition from 0-46% Ru show no individual rutile or anatase phase reflections (**Figure S10**). Overall, the absence of discernible reflections from the TiO_2-RuO_2 films suggests that the ALD-grown alloys lack long-range crystalline order.

Finally, the optical properties of these films were characterized by ultraviolet-visible (UV-vis) spectroscopy. Absorbance spectra from 200-1800 nm were collected for 10 nm alloy films ranging from 13-46% Ru grown on fused quartz substrates (**Figure S11**). Increased absorbance in the visible region is observed for higher % Ru alloys. A similar effect is observed for nitrogen doping of TiO_2 films,[38,39] providing additional evidence that RuO_2 is incorporated into the TiO_2 lattice uniformly, as opposed to in discrete islands. Nevertheless, absorbance losses for 10 nm films were minimal. At 550 nm, 90% of the light is still transmitted for a 21% TiO_2-RuO_2 alloy, which showed the highest absorption among all the alloy compositions at this wavelength.

2.2 CONDUCTIVITY OF TiO_2-RuO_2 ALLOY FILMS

In order for TiO_2-RuO_2 alloys to set the built-in field, they must be sufficiently conductive to induce the necessary band banding in the semiconductor. TiO_2-RuO_2 conductivity is assessed by measuring the half peak-to-peak (HP2P) splitting of the ferri/ferrocyanide (FFC) redox couple

using cyclic voltammetry, $E_{HP2P} = E_{peak} - E_{1/2}$ where $E_{1/2}$ is the average of the cathodic and anodic peak potentials $[(E_{pa} + E_{pc})/2]$. A lower half peak-to-peak splitting indicates higher conductivity of the ALD alloy layer. **Figure 5** compares the HP2P splitting in FFC of TiO_2-RuO_2 alloy films and non-alloyed TiO_2 films with and without an iridium coating. When iridium is used, the HP2P splitting of an 18 nm 21% Ru alloy (solid red) is already more conductive than a 7 nm TiO_2 film (solid blue). More significantly, the alloy films can function as metallic electrodes themselves, without an iridium layer. An 18 nm 21% Ru alloy (dashed red) has a HP2P of 117 mV, which is only slightly higher than the lowest HP2P values of 70-80 mV typically observed for Ir / 2 nm SiO_2 / p^+Si anodes. TiO_2 alone is unable to mediate electron transfer in FFC,[1] as indicated by the horizontal dashed blue line in **Figure 5**.

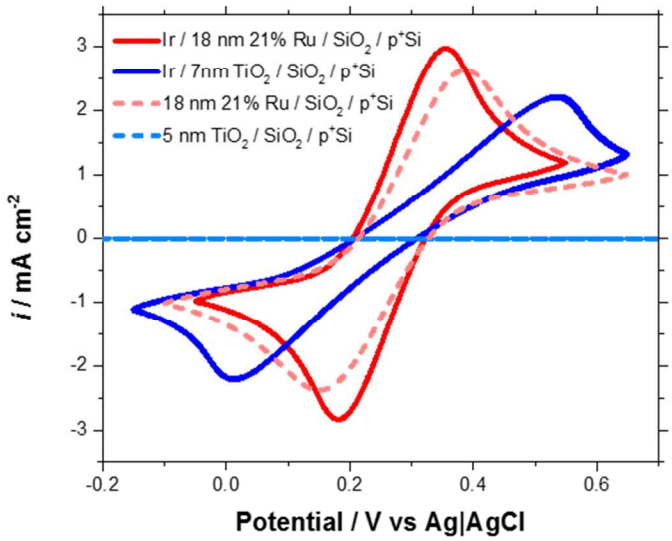

Figure 5. Half peak-to-peak (HP2P) splitting in 10 mM ferri/ferrocyanide, 1 M KCl of ALD films with (solid) and without (dashed) an iridium contact layer. The TiO_2-RuO_2 alloy films (red) are significantly more conductive than TiO_2 alone (blue), as evidenced by the smaller HP2P. Moreover, TiO_2 without iridium exhibits no electrochemical response.

In fact, the HP2P splitting shows very little dependence on thickness for a wide range of alloy compositions. **Figure 6A** shows the HP2P splitting as a function of TiO_2-RuO_2 alloy film thickness for compositions ranging from 16-46% RuO_2 on p^+Si. Film thickness was varied from 3-45 nm. Although thin compared to the dimensionally stable anode (DSA), this range encompasses the extremes of typical ALD processes. No iridium layer is used in these measurements, so the alloys themselves are functioning as the working electrode. The HP2P splitting is low and relatively constant for 21-46% Ru alloys. The HP2P increases dramatically when the alloy composition drops to 16 % Ru at all thicknesses.

As shown in **Figure 6B**, however, the addition of an iridium layer significantly reduces the HP2P of TiO_2-RuO_2 alloys with ≤ 16% Ru. This suggests that the increase in HP2P splitting observed when no iridium layer is used is most likely caused by insufficient Ru coverage at the surface to mediate efficient charge transfer to the ferri/ferrocyanide redox couple, and not by increased bulk resistivity of the alloy film. A metal layer is necessary to provide mediating electronic states at the electrolyte interface.[1] Without such a layer present, no observable Fe(II)/Fe(III) redox waves are observed (**Figure 5**, light blue dashed).[1] The increased HP2P splitting observed for low % Ru alloys is an intermediate case between these two extremes. Depositing a metal layer restores sufficient density of states at the electrode surface to mediate charge transfer, and Ru ions facilitate hole conduction through the bulk of the film. TiO_2-RuO_2 films with only 13% RuO_2 do not contribute significant series resistance when a top metal contact is used.

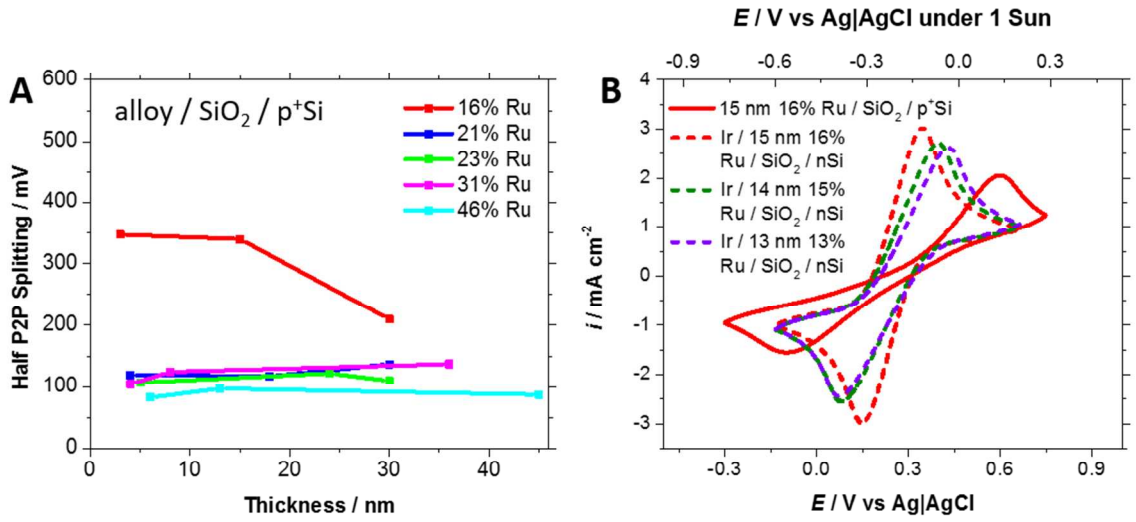

Figure 6. (A) Half peak-to-peak splitting (HP2P) for TiO_2-RuO_2 alloys as a function of film thickness for compositions ranging from 16-46% Ru. All alloys were grown on p^+Si, and the HP2P was measured in 10 mM ferri/ferrocyanide, 1 M KCl **(B)** Cyclic voltammetry measurements comparing TiO_2-RuO_2 alloy films with and without the presence of an iridium overlayer. The alloy sample measured without iridium was deposited on p^+Si and is plotted with respect to the bottom x-axis. The alloy samples measured with iridium were deposited on nSi and are plotted with respect to the top x-axis. The total range of both axes are the same, and the max/min values were chosen to place the center of each voltammmogram in the same location (since the nSi devices are shifted to negative potentials due to the photovoltage). The HP2P was again measured in 10 mM ferri/ferrocyanide, 1 M KCl, and the nSi measurements were performed under 1.5 AMG 1 sun illumination.

Overall, these electrochemical results demonstrate that TiO_2-RuO_2 alloys are highly conductive. At higher Ru concentrations, they behave like metallic conductors. As the Ru concentration

decreases, they begin to lack sufficient density of states to mediate charge transfer at the surface but are not sources of significant bulk series resistance.

2.3 HIGHLY CONDUCTIVE TiO_2-RuO_2 ALLOY CONTACTS ENABLE HIGH PHOTOVOLTAGE

Electrochemical measurements in ferri/ferrocyanide were performed to determine whether TiO_2-RuO_2 alloy Schottky contacts would enable high photovoltages. **Figure 7A** shows cyclic voltammetry data for a representative Ir/TiO_2-RuO_2 alloy/SiO_2/nSi anode in AM1.5 light compared to a Ir/TiO_2-RuO_2 alloy/SiO_2/p^+Si anode in the dark. All samples possess a native SiO_2 of approximately 2 nm in thickness, as measured by ellipsometry. The dashed line indicates the average $E_{1/2}$ across all 8 samples measured in the series. The box centered about the dashed line represents the variation in $E_{1/2}$ at the 95% confidence interval. All samples exhibit large photovoltages averaging 525 mV. The maximum photovoltage recorded was 549 mV for a 36 nm 31% RuO_2 alloy, and the minimum photovoltage recorded was 489 mV for a 13 nm 46% RuO_2 alloy. Similar photovoltages were obtained without the iridium catalyst layer, as shown in **Figure 7B**. This confirms that the built-in field, which controls the photovoltage, is set by the TiO_2-RuO_2 alloy, and not by the catalyst layer.

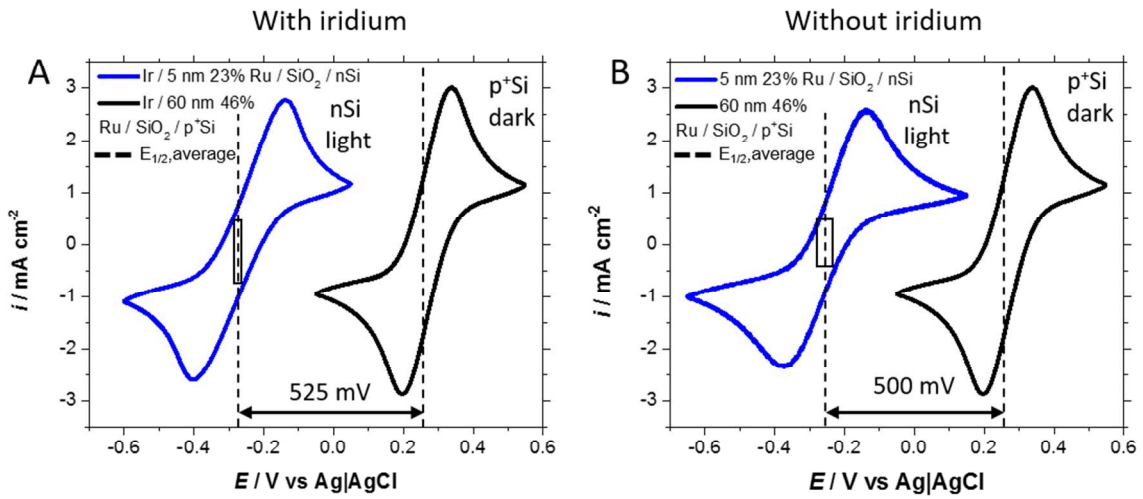

Figure 7. (A) Electrochemical performance of Ir/TiO_2-RuO_2/SiO_2/n-Si anodes in one sun AM1.5 light compared to Ir/TiO_2-RuO_2/SiO_2/p^+-Si anode in the dark. **(B)** Electrochemical performance of TiO_2-RuO_2/SiO_2/n-Si anodes in one sun AM1.5 light without the iridium catalyst compared to the Ir/TiO_2-RuO_2/SiO_2/p^+-Si anode in the dark. The dashed lines indicate the average $E_{1/2}$ across all samples. The box centered about the dashed line represents the variation in $E_{1/2}$ at the 95% confidence interval. The photovoltage for each nSi anode was calculated by comparing the $E_{1/2}$ of the p^+Si anode in the dark to the $E_{1/2}$ of the nSi anode in the light. The average photovoltage across the series was calculated to be 525 mV with iridium and 500 mV without iridium.

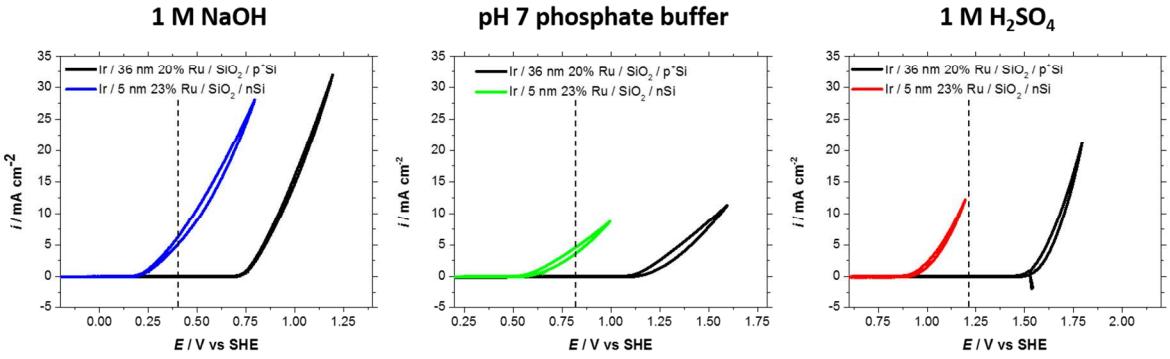

Figure 8. Water oxidation curves in 1M NaOH, pH 7 phosphate buffer, and 1 M H_2SO_4 for a representative Ir/TiO_2-RuO_2 alloy/SiO_2/nSi photoanode under 1 sun AM1.5 illumination compared to the analogous p^+Si anode measured in the dark.

The corresponding water oxidation data for Ir/TiO_2-RuO_2/SiO_2/n-Si under 1 sun AM1.5 illumination are shown in **Figure 8**. In different pH solutions, similar average photovoltages are observed during water oxidation at 1 mA cm^{-2}: 504 mV ± 21 mV in 1 M NaOH, 534 mV ± 38 mV in pH 7 phosphate buffer, and 539 mV ± 25 mV in 1 M H_2SO_4 for all eight samples in the series. Water oxidation data with saturated photocurrent are shown in **Figure S14**.

To confirm the performance of TiO_2-RuO_2 alloys as high work function, metallic Schottky contacts, capacitance voltage (CV) analysis of solid state capacitor structures was used to extract the work function for various alloy compositions. **Figure 9A** shows the structure of n and p-type MOS capacitors fabricated for this study. Aluminum, which has a reported work function of 4.1-4.2 eV,[20] was chosen as the gate metal for both n and pSi capacitors. The flatband voltage is determined by the difference between the metal and semiconductor work function, taking fixed charges, mobile charges, and interface traps into account.[40] When no TiO_2-RuO_2 alloy is present in the MIS structure, the flatband voltage should be set by the work function of the aluminum top electrode. When ALD-grown alloys are introduced, however, the flatband voltage should reflect the work function of the conductive alloy film. As a high work function (ϕ_M) is expected for the TiO_2-RuO_2 alloy, the flatband voltage should shift to more positive gate bias when such an alloy film is introduced into the capacitor stack, indicating a higher ϕ_M. **Figures 9B** and **9C** show that

such a shift is indeed observed. The flatband voltage shifts to higher gate bias by 0.7 V on pSi and 0.8 V on nSi.

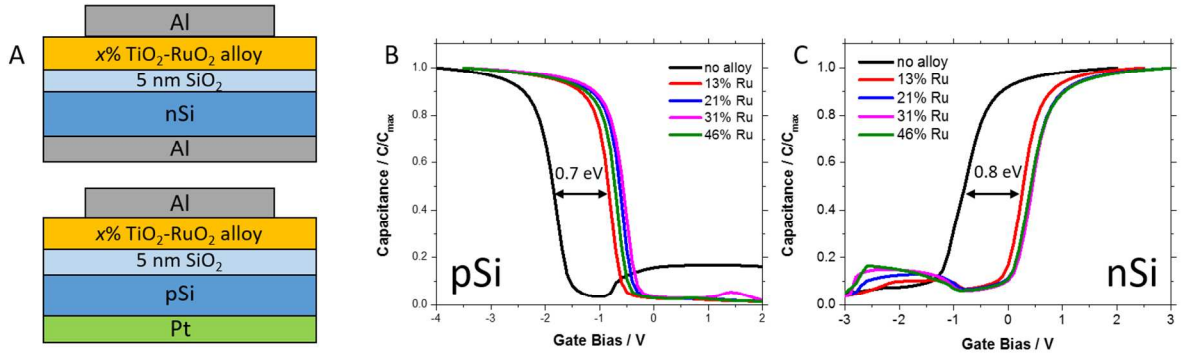

Figure 9. (A) Structure of n and pSi MOS capacitors. Aluminum was used as the gate metal in all cases. Aluminum and platinum were used to make Ohmic contacts to the back side of n and pSi substrates, respectively. **(B)** Capacitance-voltage (CV) curves for pSi MOS capacitors. **(C)** CV curves for nSi MOS capacitors. All CV curves were measured at a frequency of 1 MHz. The aluminum electrode dot diameter was 250 μm. Since the alloys are highly conductive, the Al metal does not always define the capacitor area. As a result, the measured capacitance has been scaled to 1 for clarity. More detailed analysis of the CV curves is presented in the Supporting Information.

The work function of the TiO_2-RuO_2 alloys was calculated from the observed flatband voltages. The details of these calculations are described in the Supporting Information, but briefly, the amount of fixed charge in the SiO_2 was extracted from control samples with the structure Al / 5 nm SiO_2 / Si capacitors, using an Al work function of 4.1 eV. Assuming that the ALD process does not affect the fixed oxide charge density in the SiO_2, the work functions of TiO_2-RuO_2 alloy layers ranging from 16-46% Ru were calculated to be 5-5.2 eV. These values are reported in **Table 2.**

Table 2: Calculated work function of TiO_2-RuO_2 alloys of varying % Ru deposited on n and pSi with 5 nm thermally grown SiO_2.

% Ru	φ_M on pSi	φ_M on nSi
0	4.08 (Al)	4.08 (Al)
13	5.05	5.11
21	5.19	5.20
31	5.26	5.26
46	5.28	5.21

The TiO_2-RuO_2 alloys exhibit a work function in the same range as reported for RuO_2. The work function of fully stoichiometric RuO_2 is reported to be > 5.0 eV.[41,42] It is also highly sensitive to the Ru oxidation state. In many cases, low temperature oxygen anneals are used to increase the work function.[41] Annealing under more reducing conditions has been shown to decrease the work function, either by formation of hydroxyls at the interface[43,44] or by complete reduction of RuO_2 back to Ru.[41] In the ALD-grown alloy layers, we hypothesize that depositing TiO_2 concurrently with Ru may favor the deposition of RuO_2 over metallic Ru by providing a more oxygen-rich environment. In addition to its high work function, RuO_2 is also a conductive oxide. It has a low resistivity of 35.2 ± 0.5 μΩ cm at room temperature.[45] Thus, TiO_2-RuO_2 alloys can simultaneously achieve both high conductivity and high photovoltage.

For the composition range explored in this study, the work function does not seem to strongly depend on % Ru. Alloy work functions that are independent of composition have previously been attributed to some degree of surface phase segregation between the components.[46] For example, in the Cu-Ni system, a linear dependence of the work function on % Cu is only observed after sputter removal of the surface layers. However, the photovoltage obtained from these TiO_2-RuO_2 alloys shows no measurable dependence on % Ru, indicating that the work function does not vary significantly over the composition range investigated. Further experiments at lower % Ru are necessary to fully characterize the effect of composition on the work function and conductivity of these amorphous ALD-grown TiO_2-RuO_2 alloys.

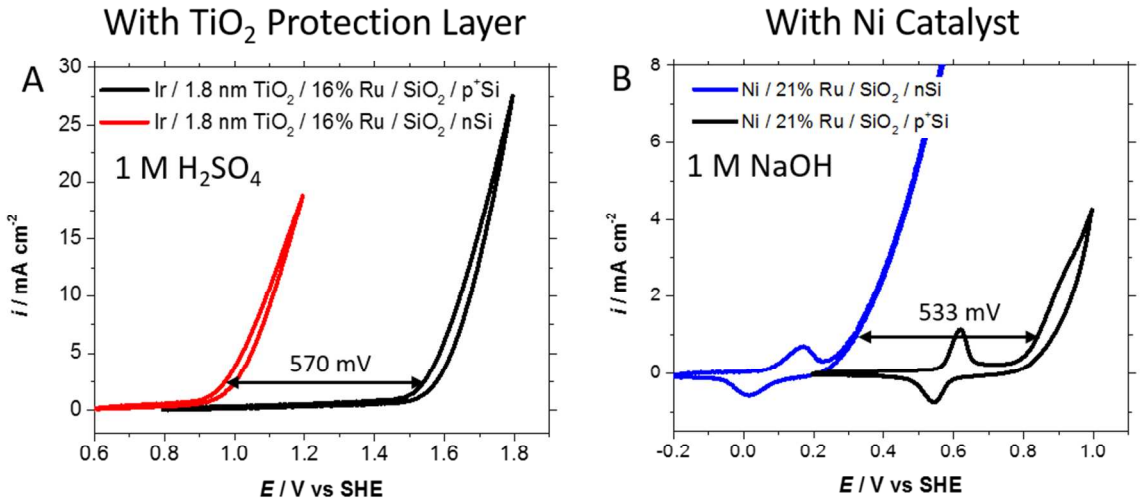

Figure 10. **(A)** Representative water oxidation data in 1 M H_2SO_4 for nSi samples in the light compared to p^+Si samples in the dark in which a 1.8 nm TiO_2 protection layer has been incorporated above the 10 nm 21% Ru alloy layer. The photovoltage is indicated at 2 mA/cm^2 for clarity. **(B)** Representative water oxidation data in 1 M NaOH for nSi samples in the light compared to p^+Si samples in the dark using a nickel catalyst on a 10 nm 21% Ru alloy. The photovoltage is indicated at 1 mA/cm.^{2}

Because the work function is set by the TiO_2-RuO_2 alloy film, the photovoltage of the resulting MIS Schottky junctions does not change when a TiO_2 protection layer is incorporated or when the surface catalyst identity is changed. **Figure 10A** shows water oxidation data in 1 M H_2SO_4 for nSi photoanodes tested in the light compared to p^+Si photoanodes in the dark in which a 1.8 nm TiO_2 protection layer was deposited on top of the TiO_2-RuO_2 alloy layer. TiO_2 overlayer thickness was calculated from XPS measurements based on the attenuation of the Ru 3d peak originating from the alloy by the TiO_2 overlayer (**Figure S15**). At 2 mA/cm^2 (chosen for clarity in the figure), the photovoltage is still 570 mV. The average photovoltage measured in FFC was 560 mV. This represents a 170-390 mV enhancement in photovoltage compared to previous studies using highly conductive TiO_2.[2,13] Because 2 nm TiO_2 is simply a tunnel barrier,[11] its incorporation does not increase the half peak-to-peak splitting in FFC (**Figure S16**). RuO_2 is known to form soluble Ru(VIII) products at more positive potentials,[15] and incorporation of a TiO_2 protection layer would likely be necessary for long-term operation. Although extended stability tests are outside the scope of this work, 2 nm ALD TiO_2 has been shown to sufficiently protect silicon photoanodes during water oxidation.[1] **Figure 10B** shows water oxidation data in 1 M NaOH for nSi photoanodes tested in the light compared to p^+Si photoanodes in the dark using ultrathin evaporated nickel films as the oxygen evolution catalyst. Eight samples were tested using alloy films ranging from 21% to 46% Ru and film thicknesses ranging from 3-45 nm. The average photovoltage was 533 mV ± 33 mV at the 95% confidence interval. Thus, isolating the MIS junction using TiO_2-RuO_2 alloys enables high photovoltages irrespective of catalyst identity or incorporation of metal oxide protection layers.

3. CONCLUSIONS

We have demonstrated that ALD alloys of TiO_2 and RuO_2 with compositions as low as 13% Ru can be used to set the built-in field, and hence control the photovoltage, in silicon MIS photoanodes. Photovoltages above 500 mV were consistently achieved regardless of catalyst identity, presence of TiO_2 protection layers, alloy film thickness, or alloy composition. Average photovoltages of 533 mV were achieved for as-deposited anodes using a NiO_x catalyst, a significant improvement over the 180-400 mV photovoltages previously reported for silicon photoanodes without a buried p^+n homojunction. Isolating the MIS Schottky junction effectively creates an isolated photovoltaic cell in series with an efficient water oxidation catalyst. As a result, this is a promising strategy for maximizing the photovoltage in silicon MIS devices, and additional components can now be incorporated and optimized without sacrificing the photovoltage. In addition, the conductivity and work function of these alloy contacts can, in principle, be tailored for other semiconductors, particularly those which do not form high quality buried homojunctions. This work suggests that a range of conductive metal oxide Schottky contacts can be synthesized by ALD alloying.

4. EXPERIMENTAL

4.1. Silicon substrates

Heavily boron-doped (100) p-type silicon wafers (ρ = 0.001-0.002 Ω cm, thickness 505-545 μm) were used as conductive silicon substrates for electrochemical measurements in the dark. Moderately phosphorous-doped (100) n-type silicon wafers (ρ = 0.14-0.24 Ω cm, thickness 450 μm) were used for electrochemical measurements in the light. The wafers were used as-received with a 1.5-2 nm native SiO_2 layer, as measured by ellipsometry. MOS capacitors for CV analysis

were fabricated on moderately boron-doped (100) p-type silicon wafers (ρ = 1-10 Ω cm, thickness 500-550 μm) with 50 Å dry thermal oxide and on moderately phosphorous-doped (100) n-type silicon wafers (ρ = 0.20-0.40 Ω cm, thickness 500-550 μm) with 50 Å dry thermal oxide.

4.2 Atomic Layer Deposition (ALD)

All ALD films were deposited in a custom-built ALD reactor (**Figure S1**). Tetrakis(dimethylamido)titanium (TDMAT) was used as the metal precursor and water as the co-reactant.[47] The TDMAT bubbler was kept at 60 °C (oven temperature) and the water bubbler was kept at room temperature. The substrate temperature was approximately 175 °C, within the ALD window for the TDMAT system.[21,47] The precursor pulse sequence is described in the Table S1 of the Supporting Information, but briefly, the TDMAT pulse time was 3 s and the H_2O pulse time was 0.5 s. TDMAT was pulsed into a stream of N_2 carrier gas at 50 sccm, but N_2 gas was not flowed through the TDMAT bubbler itself. N_2 at 50 sccm was also used as the purge gas. The equilibrium deposition pressure was approximately 300 mTorr. The TDMAT growth rate saturates as a function of precursor pulse time (**Figure S2**), a hallmark of ALD growth.

RuO_x films were grown using bis(2,4-dimethylpentadienyl) ruthenium ($Ru(DMPD)_2$) and oxygen. This precursor was chosen because its low temperature ALD window overlaps with that of TDMAT. [22,23] The $Ru(DMPD)_2$ bubbler was kept at 60 °C (oven temperature), and the deposition temperature was 175 °C. $Ru(DMPD)_2$ is a solid with a lower vapor pressure than TDMAT, so N_2 at 50 sccm was used as a carrier gas through the bubbler. N_2 at 50 sccm was also used as the purge gas. The equilibrium deposition pressure was approximately 300 mTorr. The

precursor pulse sequence is described in Table S2 of the Supporting Information, but briefly, the $Ru(DMPD)_2$ pulse time was 60 s and the O_2 pulse time was 30 s.

To grow TiO_2-RuO_2 alloys, alternating cycles of TiO_2 and RuO_x were repeated for a specified number of super-cycles. The ratio of TiO_2 cycles to RuO_x cycles was varied to control the Ru content in the film. The number of super-cycles was varied to control the film thickness. All deposition conditions were the same as the individual ALD processes.

4.3 Determination of TiO_2 Thickness by Ellipsometry

TiO_2 thickness was measured using a Gaertner ellipsometer calibrated by cross-sectional transmission electron microscopy (TEM) analysis. Each sample was approximately 2 x 2 cm, based on the diameter of the deposition chamber and the ceramic heater's zone of uniformity. 9 points were typically measured on each sample and 95% confidence intervals were calculated for the mean thickness. After optimizing the TiO_2 depositions, a typical 6 nm film had a thickness range of 6.5 – 6.8 nm and a variation of 0.06 nm at the 95% confidence interval. A typical 12 nm film had a thickness range of 11.6 – 11.9 nm and a variation of 0.07 nm at the 95% confidence interval.

4.4 Determination of Alloy Film Thickness by X-Ray Reflectivity (XRR)

Alloy film thickness was measured by X-Ray Reflectivity using a PANalytical X'Pert Diffractometer. The incident beam optics included a graded multilayer parabolic X-ray mirror, a 1/32° divergence slit, a 10 mm mask for smaller samples, and a Ni 0.15 mm automatic beam attenuator. The diffracted beam optics included a parallel plate collimator with a 0.27° receiving

slit. PANalytical's X'Pert Reflectivity software was used to calculate film thickness from a 2Theta-Omega scan using the Fourier transform method. Scans were collected from 0-8° 2θ. The step size was 0.02° and the time per step was 0.2 s.

4.5 Determination of crystal structure by grazing incidence X-ray diffraction (GIXRD)

GIXRD spectra were collected on a PANalytical X'Pert Diffractometer. The incident beam optics included a graded multilayer parabolic X-ray mirror, a 1/2° divergence slit, a 15 mm mask for smaller samples, and a Ni 0.15 mm automatic beam attenuator. The diffracted beam optics included a parallel plate collimator. No receiving slit was used in order to maximize the signal intensity. Scans were collected from 20-80° 2θ with ω = 2.5.° The step size was 0.05° with a time per step of 1 s.

4.6 Deposition of catalyst, gate metal, and back-contact

Iridium, aluminum, and platinum were deposited by electron beam evaporation. For the MOS capacitor studies, 100 nm of Al and 20 nm of Pt was used. Al was used as the gate metal for both n and p-Si wafers. Al was used as the back contact for n-Si wafers, and Pt was used as the back contact for p-Si wafers. For the electrochemical measurements, 2 nm Ir, 100 nm Al, and 20 nm Pt were used. Again, Al was used as the back contact for all n-Si wafers, and Pt was used as the back contact for al p^+-Si wafers.

4.7 X-Ray Photoelectron Spectroscopy (XPS)

Elemental characterization of the alloy films was performed using a PHI 5000 VersaProbe^{TM} X-Ray Photoelectron Spectrometer. The chamber base pressure was typically on the order of 10^{-7}

Torr. The X-ray source was monochromatic Al Kα (1486.6 eV). The X-ray power was 50 W, and the beam diameter was focused to 200 μm. The source-analyzer angle was 45°. For survey scans, the pass energy was 117.4 eV with an energy step of 1.0 eV. For high resolution scans, the pass energy was 23.5 eV with an energy step of 0.10 eV. The time/step was 20 ms in all cases.

CasaXPS software was used for all elemental analyses and peak fitting procedures. All peak positions were referenced to the Si 2p peak at 99 eV. Relative sensitivity factors for each element were taken from the PHI Multipak Manual.

4.8 Electrochemical Measurements

The pH 7 phosphate buffer solution was made with 0.42 M Na_2HPO_4 and 0.58 M NaH_2PO_4. The pH was measured and adjusted accordingly to 7. The acidic and basic solutions were made with 1 M H_2SO_4 and 1 M NaOH, respectively. The aqueous ferri/ferrocyanide solution was made with 10 mM $K_3Fe(CN)_6$, 10 mM $K_4Fe(CN)_6$, and 1 M KCl. All electrochemical measurements were performed using a bored (5 mm diameter, 0.196 cm^2 area) Teflon cone pressed against the sample to define the electrode area and contain the electrolyte solution. A Pt wire was used as a counter electrode. A Ag(s)|AgCl(s) sat. KCl (aq) electrode purchased from BioAnalytical Systems was used as the reference electrode. Potentials measured versus Ag|AgCl were converted to SHE. All measurements were conducted using a WaveNow potentiostat in air at room temperature. Cyclic voltammograms were recorded at a scan rate of 100 mV s^{-1}. Chronoamperometry stability measurements were performed using a peristaltic pump to circulate the solution at 1 mL s^{-1}.

4.9 MOS Capacitor Fabrication and Measurements

MOS capacitors were fabricated using stencil lithography. Al gate metals were deposited through a shadow mask that defined circular capacitors of diameters ranging from 100-250 μm. All CV measurements were taken at room temperature. The gate bias was varied such that the capacitors moved from depletion to accumulation. A superimposed 25 mV AC voltage was applied at a frequency range of 1 kHz – 1 MHz.

4.10 Auger Electron Spectroscopy (AES) Mapping

AES maps were collected using a PHI 700 Auger Electron Spectrometer. For high resolution maps, a beam energy of 10 kV with 10 nA was chosen. A 2-point acquisition method was used with a resolution of 256 pixels.

4.11 Ultra-violet visible Spectroscopy (UV-vis)

UV-vis spectra were collected on a Cary 6000i UV/Vis/NIR Spectrometer in the wavelength range 200-1800 nm. A bare quartz slide was used for baseline correction. Fused quartz slides of thickness 1 mm were purchased from AdValue Technology.

4.12 Transmission Electron Microscopy (TEM)

Micro-structural analysis was performed using an HR-TEM (Jeol 2100 transmission electron microscope; 200 kV; double tilt holder). Cross-sections of the films were prepared using a FEI Dual-Beam Helios NanoLab 600i Focused Ion Beam (FIB) (final thinning at 93 pA 30 kV, final polish 5 kV 47 pA).

ASSOCIATED CONTENT

Supporting Information: Detailed methods and analysis for XPS, XRR, GIXRD, UV-vis, capacitance-voltage analysis, AES, and TEM. Also contains a detailed description of custom ALD reactor. This material is available free of charge via the Internet at http://pubs.acs.org.

AUTHOR INFORMATION

Corresponding Author

*C. E. D. Chidsey. Email: chidsey@stanford.edu

*P. C. McIntyre. Email: pcm1@stanford.edu

Author Contributions

O. H. prepared all samples and performed all experiments for this study with the aid of A. S. M. S. prepared and imaged alloy samples by transmission electron microscopy. O. H., C. E. D. C., P. H., and P. M. designed the experiments. All authors helped in the preparation of this manuscript.

Notes

The authors declare no competing financial interest.

ACKNOWLEDGMENTS

We thank T. Carver for metal e-beam evaporations and all members of the RENEW collaboration in addition to the authors: M. Pemble, A. Mills, I. Povey, J. Kegel, K. Cherkaoui, S. Monaghan, and D. Hazafy. O. H. would like to thank McIntyre group members A. Scheuermann, K. Kemp, R. Tang-Kong, A. Negara, T. Chor Seng, and W. Tang, as well as Chidsey group members S. Ramakrishnan and M. Van den Berg for insightful discussions. O. H.

would also like to thank C. Hitzman of the Stanford Nano Shared Facilities for his guidance with XPS and AES. We also acknowledge A. Vailionis for his help with XRR and GIXRD measurements. This work was partially supported by the Stanford Global Climate and Energy Project and National Science Foundation program CBET-1336844. The authors from Tyndall National Institute acknowledge the financial support of Science Foundation (SFI) under the US-Ireland R&D Partnership Program—Grant Number SFI/13/US/12543. O. H. graciously acknowledges support from the Fannie and John Hertz Foundation.

REFERENCES

(1) Chen, Y. W.; Prange, J. D.; Dühnen, S.; Park, Y.; Gunji, M.; Chidsey, C. E. D.; McIntyre, P. C. Atomic Layer-Deposited Tunnel Oxide Stabilizes Silicon Photoanodes for Water Oxidation. *Nat. Mater.* **2011**, *10* (7), 539–544.

(2) Hu, S.; Shaner, M. R.; Beardslee, J. A.; Lichterman, M.; Brunschwig, B. S.; Lewis, N. S. Amorphous TiO2 Coatings Stabilize Si, GaAs, and GaP Photoanodes for Efficient Water Oxidation. *Science* **2014**, *344*, 1005–1009.

(3) Singh, R.; Green, M. A.; Rajkanan, K. Review of Conductor-Insulator-Semiconductor (CIS) Solar Cells. *Sol. Cells* **1981**, *3* (2), 95–148.

(4) Green, M. A. Effects of Pinholes, Oxide Traps, and Surface States on MIS Solar Cells. *Appl. Phys. Lett.* **1978**, *33* (2), 178–180.

(5) Green, M. a; Blakers, a W. Advantages of Metal-Insulator-Semiconductor Structure for Silicon Solar Cells. *Sol. Cells* **1983**, *8*, 3–16.

(6) Godfrey, R. B.; Green, M. A. 655 mV Open-Circuit Voltage, 17.6% Efficient Silicon MIS

Solar Cells. *Appl. Phys. Lett.* **1979**, *34* (11), 790–793.

(7) Lichterman, M. F.; Sun, K.; Hu, S.; Zhou, X.; McDowell, M. T.; Shaner, M. R.; Richter, M. H.; Crumlin, E. J.; Carim, A. I.; Saadi, F. H.; Brunschwig, B. S.; Lewis, N. S. Protection of Inorganic Semiconductors for Sustained, Efficient Photoelectrochemical Water Oxidation. *Catal. Today* **2016**, *262*, 11–23.

(8) Kenney, M. J.; Gong, M.; Li, Y.; Wu, J. Z.; Feng, J.; Lanza, M.; Dai, H. High-Performance Silicon Photoanodes Passivated with Ultrathin Nickel Films for Water Oxidation. *Science* **2013**, *342* (6160), 836–840.

(9) Shaner, M. R.; Hu, S.; Sun, K.; Lewis, N. S. Stabilization of Si Microwire Arrays for Solar-Driven H2O Oxidation to O2(g) in 1.0 M KOH(aq) Using Conformal Coatings of Amorphous TiO2. *Energy Environ. Sci.* **2015**, *8*, 203–207.

(10) Zhou, X.; Liu, R.; Sun, K.; Friedrich, D.; McDowell, M. T.; Yang, F.; Omelchenko, S. T.; Saadi, F. H.; Nielander, A. C.; Yalamanchili, S.; Papadantonakis, K. M.; Brunschwig, B. S.; Lewis, N. Interface Engineering of the Photoelectrochemical Performance of Ni-Oxide-Coated N-Si Photoanodes by Atomic-Layer Deposition of Ultrathin Films of Cobalt Oxide. *Energy Environ. Sci.* **2015**, *8*, 2644–2649.

(11) Scheuermann, A. G.; Prange, J. D.; Gunji, M.; Chidsey, C. E. D.; McIntyre, P. C. Effects of Catalyst Material and Atomic Layer Deposited TiO2 Oxide Thickness on the Water Oxidation Performance of Metal–insulator–silicon Anodes. *Energy Environ. Sci.* **2013**, *6* (8), 2487-2496

(12) Scheuermann, A. G.; Lawrence, J. P.; Kemp, K. W.; Ito, T.; Walsh, A.; Chidsey, C. E. D.;

Hurley, P. K.; McIntyre, P. C. Design Principles for Maximizing Photovoltage in Metal-Oxide-Protected Water-Splitting Photoanodes. *Nat. Mater.* **2016**, *15* (October), 99–105.

(13) McDowell, M. T.; Lichterman, M. F.; Carim, A. I.; Liu, R.; Hu, S.; Brunschwig, B. S.; Lewis, N. S. The Influence of Structure and Processing on the Behavior of TiO_2 Protective Layers for Stabilization of N-Si/TiO_2/Ni Photoanodes for Water Oxidation. *ACS Appl. Mater. Interfaces* **2015**, *7* (28), 15189–15199.

(14) Green, M. A. Limits on the Open-Circuit Voltage and Efficiency of Silicon Solar Cells Imposed by Intrinsic Auger Processes. *IEEE Trans. Electron Devices* **1984**, *ED-31* (5), 671–678.

(15) Pourbaix, M. *Atlas of Electrochemical Equilibria in Aqueous Solutions*; 1966.

(16) Trasatti, S. Electrocatalysis: Understanding the Success of DSA®. *Electrochim. Acta* **2000**, *45* (15-16), 2377–2385.

(17) Over, H. Surface Chemistry of Ruthenium Dioxide in Heterogeneous Catalysis and Electrocatalysis: From Fundamental to Applied Research. *Chem. Rev.* **2012**, *112* (6), 3356–3426.

(18) Trasatti, S. Physical Electrochemistry of Ceramic Oxides. *Electrochim. Acta* **1991**, *36* (2), 225–241.

(19) Greiner, M. T.; Chai, L.; Helander, M. G.; Tang, W. M.; Lu, Z. H. Transition Metal Oxide Work Functions: The Influence of Cation Oxidation State and Oxygen Vacancies. *Adv. Funct. Mater.* **2012**, *22* (21), 4557–4568.

(20) Michaelson, H. B. The Work Function of the Elements and Its Periodicity. *J. Appl. Phys.*

1977, *48* (11), 4729–4733.

(21) Scheuermann, A. G.; Lawrence, J. P.; Gunji, M.; Chidsey, C. E. D.; McIntyre, P. C. ALD-TiO2 Preparation and Characterization for Metal-Insulator-Silicon Photoelectrochemical Applications. *ECS Trans.* **2013**, *58* (10), 75–86.

(22) Methaapanon, R.; Geyer, S. M.; Lee, H.-B.-R.; Bent, S. F. The Low Temperature Atomic Layer Deposition of Ruthenium and the Effect of Oxygen Exposure. *J. Mater. Chem.* **2012**, 25154–25160.

(23) Methaapanon, R.; Geyer, S. Size Dependent Effects in Nucleation of Ru and Ru Oxide Thin Films by Atomic Layer Deposition Measured by Synchrotron Radiation X-Ray Diffraction. *Chem. Mater.* **2013**, *25*, 3458–3463.

(24) Aaltonen, T.; Aløn, P.; Ritala, M.; Leskelä, M. Ruthenium Thin Films Grown by Atomic Layer Deposition. *Chem. Vap. Deposition* **2003**, *9* (1), 45–49.

(25) Aaltonen, T.; Ritala, M.; Arstila, K.; Keinonen, J.; Leskelä, M. Atomic Layer Deposition of Ruthenium Thin Films from Ru(thd)3 and Oxygen. *Chem. Vap. Deposition* **2004**, *10* (4), 215–219.

(26) Li, H.; Aaltonen, T.; Li, Z.; Lim, B. S.; Gordon, R. G.; Rd, V. Synthesis and Characterization of Ruthenium Amidinate Complexes as Precursors for Vapor Deposition. *Open Inorg. Chem. J.* **2008**, *2*, 11–17.

(27) Gregorczyk, K.; Henn-lecordier, L.; Gatineau, J.; Dussarrat, C.; Rubloff, G. Atomic Layer Deposition of Ruthenium Using the Novel Precursor bis(2,6,6-Trimethyl-Cyclohexadienyl)ruthenium. *Chem. Mater.* **2011**, *23*, 2650–2656.

(28) Kim, S. K.; Lee, S. Y.; Lee, S. W.; Hwang, G. W.; Hwang, C. S.; Lee, J. W.; Jeong, J. Atomic Layer Deposition of Ru Thin Films Using 2,4-(Dimethylpentadienyl)(ethylcyclopentadienyl)Ru by a Liquid Injection System. *J. Electrochem. Soc.* **2007**, *154*, D95.

(29) Diebold, U. TiO2 by XPS. *Surf. Sci. Spectra* **1996**, *4* (3), 227.

(30) Jensen, D. S.; Kanyal, S. S.; Madaan, N.; Vail, M. A.; Dadson, A. E.; Engelhard, M. H.; Linford, M. R. Silicon (100)/SiO2 by XPS. *Surf. Sci. Spectra* **2013**, *20* (1), 36–42.

(31) Morgan, D. J. Resolving Ruthenium: XPS Studies of Common Ruthenium Materials. *Surf. Interface Anal.* **2015**, *47* (11), 1072–1079.

(32) Kaga, Y. Ru and RuO2 Thin Films by XPS. *Surf. Sci. Spectra* **1999**, *6* (1), 68.

(33) Kim, Y. J.; Gao, Y.; Chambers, S. a. Core-Level X-Ray Photoelectron Spectra and X-Ray Photoelectron Diffraction of RuO2(110) Grown by Molecular Beam Epitaxy on TiO2(110). *Appl. Surf. Sci.* **1997**, *120*, 250–260.

(34) Mun, C.; Ehrhardt, J. J.; Lambert, J.; Madic, C. XPS Investigations of Ruthenium Deposited onto Representative Inner Surfaces of Nuclear Reactor Containment Buildings. *Appl. Surf. Sci.* **2007**, *253* (18), 7613–7621.

(35) Oh, S.; Park, C.; Park, C. Thermal Stability of RuO 2/Ru Bilayer Thin Film in Oxygen Atmosphere. *Thin Solid Films* **2000**, *359*, 118–123.

(36) Todorova, M.; Li, W. X.; Ganduglia-Pirovano, M. V.; Stampfl, C.; Reuter, K.; Scheffler, M. Role of Subsurface Oxygen in Oxide Formation at Transition Metal Surfaces. *Phys. Rev. Lett.* **2002**, *89* (9), 096103.

(37) Naslund, L.-A.; Sanchez-Sanchez, C. M.; Ingason, A. S.; Backstrom, J.; Herrero, E.; Rosen, J.; Holmin, S. The Role of TiO2 Doping on RuO2 -Coated Electrodes for the Water Oxidation Reaction. *J. Phys. Chem. C* **2013**, *117* (12), 6126–6135.

(38) Islam, S. Z.; Reed, A.; Kim, D. Y.; Rankin, S. E. N2/Ar Plasma Induced Doping of Ordered Mesoporous TiO2 Thin Films for Visible Light Active Photocatalysis. *Microporous Mesoporous Mater.* **2016**, *220*, 120–128.

(39) Asahi, R.; Morikawa, T.; Ohwaki, T.; Aoki, K.; Taga, Y. Visible-Light Photocatalysis in Nitrogen-Doped Titanium Oxides. *Science* **2001**, *293*, 269–272.

(40) Schroder, D. K. Electrical Characterization of Defects in Gate Dielectrics. In *Defects in Microelectronic Materials and Devices*; Fleetwood, D. M., Pantelides, S. T., Schrimpf, R. D., Eds.; CRC Press, 2009.

(41) Park, C. S.; Bersuker, G.; Hung, P. Y.; Kirsch, P. D.; Jammy, R. Impact of Oxygen on Work Function of Ru Oxide Metal Gate. *Electrochem. Solid-State Lett.* **2010**, *13* (4), H105–H107.

(42) Pantisano, L.; Schram, T.; Li, Z.; Lisoni, J. G.; Pourtois, G.; Gendt, S. De; Brunco, D. P.; Akheyar, A.; Afanas, V. V; Shamuilia, S.; Stesmans, A.; Pantisano, L.; Schram, T.; Li, Z.; Lisoni, J. G.; Pourtois, G.; Gendt, S. De. Ruthenium Gate Electrodes on SiO2 and HfO2 : Sensitivity to Hydrogen and Oxygen Ambients. *Appl. Phys. Lett.* **2012**, *88*, 243514.

(43) Sun, Q.; Reuter, K.; Scheffler, M. Hydrogen Adsorption on RuO2(110): Density-Functional Calculations. *Phys. Rev. B - Condens. Matter Mater. Phys.* **2004**, *70* (23), 1–12.

(44) Sun, Q.; Reuter, K.; Scheffler, M. Effect of a Humid Environment on the Surface Structure of RuO2 (100). *Phys. Rev. B* **2003**, *67* (20), 205424.

(45) Ryden, W. D.; Lawson, A. W. Electrical Transport Properties of IrO2 and RuO2. *Phys. Rev. B* **1970**, *1* (4), 1494–1500.

(46) Rothschild, J. A.; Eizenberg, M. Work Function Calculation of Solid Solution Alloys Using the Image Force Model. *Phys. Rev. B* **2010**, *81*, 224201–1 – 224201–224208.

(47) Yun, J.; Park, M.; Rhee, S. Comparison of Tetrakis (dimethylamido) Titanium and Tetrakis (diethylamido) Titanium as Precursors for Metallorganic Chemical Vapor Deposition of Titanium Nitride. *J. Electrochem. Soc.* **1999**, *146* (5), 1804–1808.

TOC GRAPHIC